PNAS RESEARCH ARTICLE | CHEMISTRY

Lithiating magneto-ionics in a rechargeable battery

Yong Hu[a], Weiyi Gong[b], Sichen Wei[c], Saurabh Khuje[a], Yulong Huang[a], Zheng Li[a], Yuguang C. Li[d,1], Fei Yao[c,1], Qimin Yan[b,1], and Shenqiang Ren[a,d,e,1]

Edited by Alexis Bell, University of California, Berkeley, CA; received December 17, 2021; accepted March 8, 2022

Magneto-ionics, real-time ionic control of magnetism in solid-state materials, promise ultralow-power memory, computing, and ultralow-field sensor technologies. The real-time ion intercalation is also the key state-of-charge feature in rechargeable batteries. Here, we report that the reversible lithiation/delithiation in molecular magneto-ionic material, the cathode in a rechargeable lithium-ion battery, accurately monitors its real-time state of charge through a dynamic tunability of magnetic ordering. The electrochemical and magnetic studies confirm that the structural vacancy and hydrogen-bonding networks enable reversible lithiation and delithiation in the magnetic cathode. Coupling with microwave-excited spin wave at a low frequency (0.35 GHz) and a magnetic field of 100 Oe, we reveal a fast and reliable built-in magneto-ionic sensor monitoring state of charge in rechargeable batteries. The findings shown herein promise an integration of molecular magneto-ionic cathode and rechargeable batteries for real-time monitoring of state of charge.

magneto-ionics | sensor | lithium-ion battery | state of charge | molecule-based magnet

Significance

Magneto-ionics promise ultralow-field sensor technologies. Meanwhile, the extent of real-time ion insertion/extraction of an electrode is the key state-of-charge (SOC) feature in batteries. We report lithiating magneto-ionic material to enable the precise SOC sensor monitoring in Li-ion battery using a molecular magnetic electrode. A microwave-excited spin wave reveals the lithiation level in the molecular-magnetic cathode, enabling precise magneto-ionic-based SOC monitoring under a lowest frequency and magnetic field of 0.35 GHz and 100 Oe, respectively, significantly lower than that of an inorganic magnetic electrode. More importantly, the magneto-ionic-based sensor shows a more than 2,000% increase in accuracy and a more than 5,000% reduction in response time. The findings provide the pathway toward the real-time accurate SOC estimation using molecular magnetic electrode.

Magneto-ionic materials rely on ionic conduction and immobilization to tune their real-time magnetism (1–4), while the ion insertion/extraction in battery electrode materials are the key feature in rechargeable batteries in controlling their real-time state of charge (SOC). However, it is challenging to precisely monitor the real-time SOC due to the complex parameters involved in charging/discharging of rechargeable batteries (*SI Appendix*, Table S1). To enable the real-time SOC using magneto-ionics, we surmised the following design parameters: 1) magneto-ionic material should be an ion conductor with reversible valence states to enable the ion insertion and extraction; 2) the extent of ion insertion/extraction and magneto-ionics should be bijective for the SOC estimation; and 3) the monitoring of ionic-responsive magnetism should be compatible with the operation of batteries. Here, we report magneto-ionic cathode material, compound 1 ($V[Cr(CN)_6]_{0.85}\cdot 1.74H_2O$; *SI Appendix*, Figs. S1 and S2), to monitor real-time SOC through reversible lithiation and delithiation in a lithium-ion (Li-ion) battery. Recent years have witnessed a shift toward responsive molecular hybrid materials due to their lightweight character, synthetic versatility, structural vacancy, and low Gilbert damping (5–11). The structural vacancy of such a porous network could induce mass transfer (such as proton and alkali metal ions), promising magneto-ionic control of its magnetism (12–17) and gaining attention as the electrode material in Li-ion batteries. The structural vacancy networks, serving as the ion migration channels, enable a high ionic conductivity (Fig. 1 *B*, Inset) to avoid the space charge zone and promote diffusion kinetics (18). Fourier transform infrared spectroscopy (FTIR) and computational modeling further suggest that the ionic control of magnetism in such a compound can be ascribed to the redox behavior of transition metal ions. Radiofrequency (RF)-based ferromagnetic resonance (FMR) excites the spin wave to monitor lithiation-controlled magneto-ionics (Fig. 1*A*), paving the way for the real-time SOC evaluation in Li-ion batteries at a low frequency and a magnetic field of 0.35 GHz and 100 Oe, respectively (Fig. 1*B*), significantly lower than that of an inorganic magnetic electrode. As compared to terminal voltage and open-circuit voltage (OCV)-based approaches, the magneto-ionic-based sensor has a more than 20-fold improvement in accuracy and a more than 50-fold decrease in response time.

Results

To examine the reversible Li insertion/extraction in magnetic compound 1 cathode material, we show a typical potential versus capacity profile for a stable charge/discharge cycle with respect to Li metal after activation (Fig. 2*A* and *SI Appendix*, Fig. S3) (19–21). The operating Li intercalation and deintercalation voltage of compound 1 is centered on approximately 1.5 V versus Li/Li^+. Fig. 2*B* shows rate performance of compound 1 as a cathode material at various C rates. The discharge capacity reaches 153 mAh g^{-1} under 0.1 C rate. Even with a high 10 C discharge rate, the electrode

Author contributions: Y. Hu and S.R. designed research; Y. Hu, W.G., and S.W. performed research; Y. Hu, S.K., Y. Huang, and Z.L. contributed new reagents/analytic tools; Y. Hu, W.G., S.W., Y.C.L., F.Y., Q.Y., and S.R. analyzed data; and Y. Hu, W.G., Y.C.L., F.Y., Q.Y., and S.R. wrote the paper.

The authors declare no competing interest.

This article is a PNAS Direct Submission.

[1]To whom correspondence may be addressed. Email: yuguangl@buffalo.edu, feiyao@buffalo.edu, qiminyan@temple.edu, or shenren@buffalo.edu.

This article contains supporting information online at http://www.pnas.org/lookup/suppl/doi:10.1073/pnas.2122866119/-/DCSupplemental.

Published June 13, 2022.

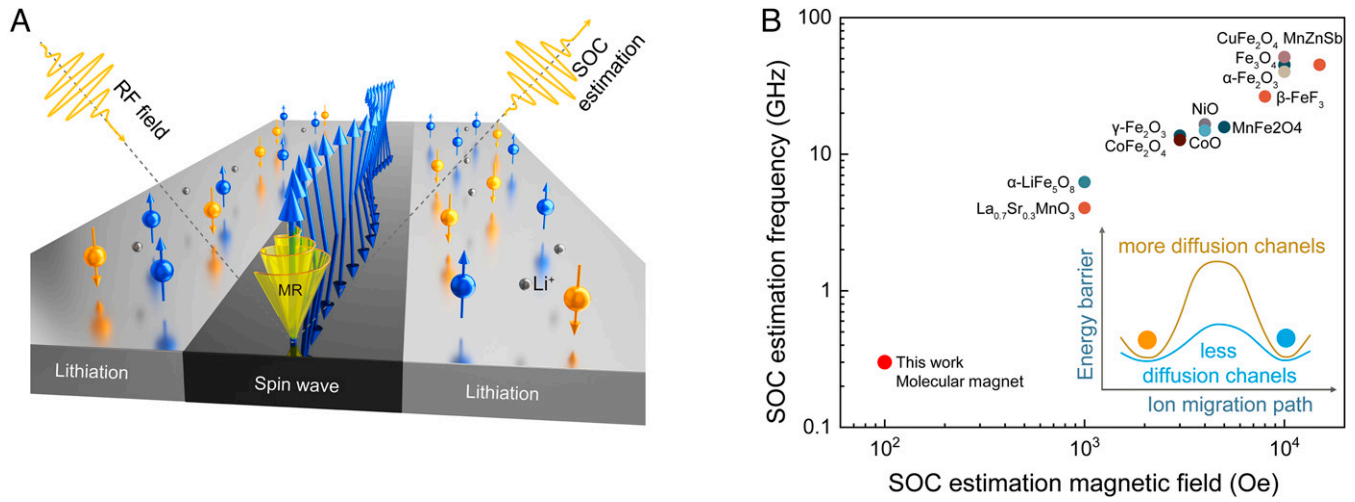

Fig. 1. Molecular magneto-ionics for monitoring SOC in rechargeable Li-ion battery. (*A*) Illustration of magneto-ionic-based SOC estimation. The incident RF field could excite a spin wave in the molecular magnet electrode at FMR condition, causing a change in the outgoing RF field. The change in the outgoing RF field is correlated with the lithiation level, proving a way for monitoring the SOC in a Li battery. (*B*) The required lowest RF field frequency (SOC estimation frequency) and magnetic field (SOC estimation magnetic field) for magnetic electrode-based SOC estimation in a Li battery (*SI Appendix*, Table S2). (*Inset*) The ion migration energy landscape. The molecular magnet shows more diffusion channels due to its unique vacancy structure, which results in a large ionic conductivity for the Li battery. According to the following equation, the low saturated magnetization (M_s) and resonance field (H_{res}) values of such a molecular magnet are beneficial for obtaining a low microwave frequency: $f = \frac{g\mu_0\mu_B}{h}\sqrt{H_{res}\,(H_{res}+M_s)}$. Here, f is the RF for magnetic resonance at H_{res}, μ_B is Bohr magneton, μ_0 is vacuum permeability, and h is Planck's constant (12, 13, 23, 36).

material still provides 20 mAh g^{-1} capacity. When returning to 0.1 C rate, the capacity recovers to 144 mAh g^{-1}, indicating the stable cycling of compound 1 as electrode material. In Fig. 2*C*, we performed electrochemical impedance spectroscopy (EIS) on compound 1 at different discharge voltages to further understand its charge/discharge kinetics. The EIS results are fitted with an equivalence circuit (Fig. 2 *C*, Inset). The series resistor (R_s), representing the ohmic resistance of the electrode assembly, does not show an obvious change with the SOC. The charge-transfer resistance (R_{ct}) between the electrode and electrolyte is fitted to be around 40 Ω at 2.5, 2, and 1.5 V. Upon lithiation to 1 and 0.5 V, R_{ct} increases significantly to 88 and 103 Ω, respectively. This is consistent with the expectation of a battery intercalation material at 0.5 V versus Li/Li^+, when

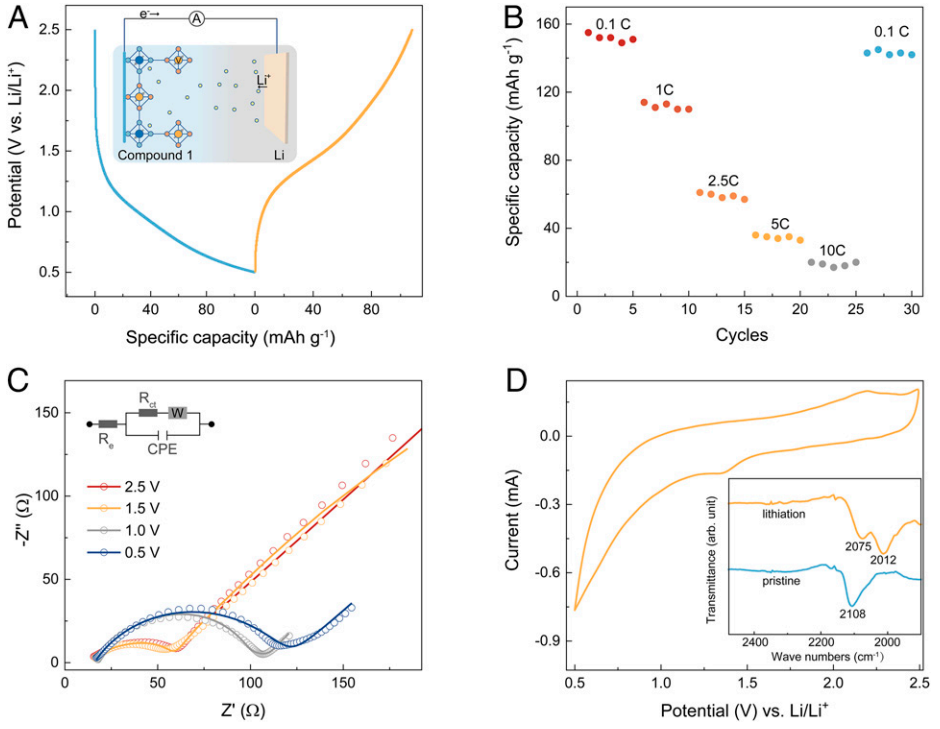

Fig. 2. Electrochemical performance and kinetic analysis of the compound 1–based electrode. (*A*) The discharge-charge curve for compound 1–based Li-ion battery under 1 C rate. (*Inset*) The relationship between magnetization control and the lithiation/delithiation reaction in the Li-ion battery (Li/compound 1). (*B*) The rate performance of the electrodes at different C rates. (*C*) Nyquist plots for compound 1 at different lithiation levels. The Nyquist plot consists of a high-frequency series resistor (R_s), a medium-frequency depressed semicircle associated with charge-transfer resistance (R_{ct}), a low-frequency linear part corresponding to the Warburg diffusion region (W), and a constant phase element. (*D*) Cyclic voltammetry curve for compound 1 at 10 mV s^{-1}. (*Inset*) The FTIR spectra for pristine compound 1 and after lithiation.

compound 1 is full of Li-ion within its lattice; a larger charge transfer resistance is expected in order to further intercalate excess Li-ion. Fig. 2*D* shows the cyclic voltammetry curve of compound 1 at a scan rate of 10 mV s^{-1}, evidencing the insertion and extraction of Li-ions. The peak observed around 1.3 V versus Li/Li^+ corresponds to the reduction of $[Cr^{III}(CN)_6]^{3-}$ to $[Cr^{II}(CN)_6]^{4-}$ with the corresponding oxidation taking place at 2.2 V versus Li/Li^+ (22). The redox feature observed during the cyclic voltammogram can be matched roughly to the charging/discharging plateau during the cycling (Fig. 2*A*). Furthermore, the vibrational shift of the compound is also supported by the ex situ FTIR measurement (Fig. 2 *D*, Inset). The peak at 2,108 cm^{-1} corresponds to the C≡N bond, while upon lithiation, it disappears; meanwhile, two new peaks emerge at lower wavenumbers of 2,075 and 2,012 cm^{-1}, suggesting the deformation of the C≡N groups due to the reduction of $[Cr^{III}(CN)_6]^{3-}$ (23).

The structural vacancy in compound 1 enables the insertion and extraction of Li ions (24–26), which, in turn, leads to the dynamic and reversible tuning of magnetic exchange interactions in compound 1. Fig. 3*A* shows the temperature-dependent magnetization of compound 1 during the Li insertion/extraction. Before lithiation, it shows a typical magnetic transition between low-temperature ferrimagnetic phase and high-temperature paramagnetic phase with a critical temperature (T_c) of 317 K (7, 27, 28). The T_c of compound 1 decreases to 220 K at a lithiation level of 115 mAh g^{-1}, while after delithiation, the T_c of compound 1 can be restored to 315 K. Fig. 3*B* shows the room-temperature magnetic hysteresis loops for compound 1 measured at different states of charge. The saturated magnetization is decreased from 1.07 to 0.04 emu g^{-1} with the lithiation to a level of 115 mAh g^{-1}. The Li-cation insertion–induced magnetic response in compound 1 can be reversible. After delithiation, the saturated magnetization is restored to 1.03 emu g^{-1}, close to its original value.

The FMR measurements are further performed to study magneto-ionic control in compound 1. Fig. 3*C* shows the broadband FMR derivative spectrum under various microwave frequencies. The resonance microwave frequency and magnetic field show a linear relationship. At 0.35 GHz microwave source, a very low resonance magnetic field of 126 Oe is obtained. The narrow peak-to-peak width, ΔH, of ∼56.2 Oe at 0.35 GHz (*SI Appendix*, Fig. S4) indicates its homogeneity. We further perform in situ FMR measurements during the lithiation process under 0.35-GHz microwave frequency to confirm that Li intercalation and magnetic performance are bijective. As shown in Fig. 3*D*, the FMR signal becomes weaker as more Li ions are intercalated into compound 1, and the FMR signal disappears at a discharging level of 117 mAh g^{-1}, suggesting that room-temperature ferrimagnetic phase is fully switched to the paramagnetic phase.

First-principle calculations based on density-functional theory (DFT), using a material model of $Li_xV_8[Cr(CN)_6]_7{\cdot}14H_2O$ ($x = 0, 8$; Fig. 4 *A* and *B*), provide a mechanistic understanding of its magneto-ionic control, on which the compound undergoes a large lattice expansion after Li insertion (*SI Appendix*, Table S3) due to the change in charge distribution (Fig. 4 *C* and *D*). The lattice expansion occurs along all three lattice directions during the insertion of Li ions, which results in a total volume change of 2.88% (*SI Appendix*, Table S4). It should be noted that the vacancies in the lattice provide pathways for Li-ion migration. *SI Appendix*, Fig. S5*A* shows the ligand and zeolitic water molecules cooperatively form a network through hydrogen bonds, providing a fast conducting network based on the diffusion-free Grotthuss mechanism (29). The water network–mediated electron migration mechanism can be supported by the increase in charge transfer resistance after lithiation due to the breaking of hydrogen-bonded percolation network (Fig. 2*C* and *SI Appendix*, Fig. S5*B*). Fig. 3 *E* and *F* show the spin-polarized projected density of states onto

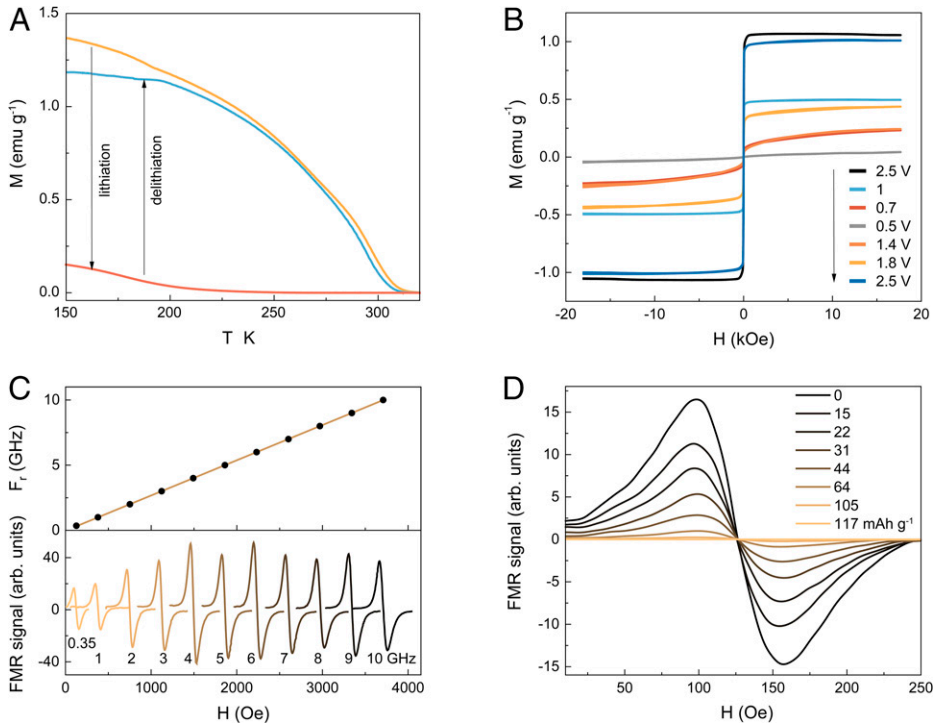

Fig. 3. Magneto-ionic switching of magnetization for compound 1. (*A*) Temperature dependence of magnetization for compound 1 after lithiation and delithiation. (*B*) Magnetic hysteresis loops of the experimental device that was discharged and charged at different levels during the first discharge-charge process. (*C*) Room-temperature FMR spectra at different RF conditions and the resonance frequency as a function of resonance field for compound 1. (*D*) Room-temperature FMR spectra under 0.35 GHz for compound 1 cathode inside the battery at different discharge levels.

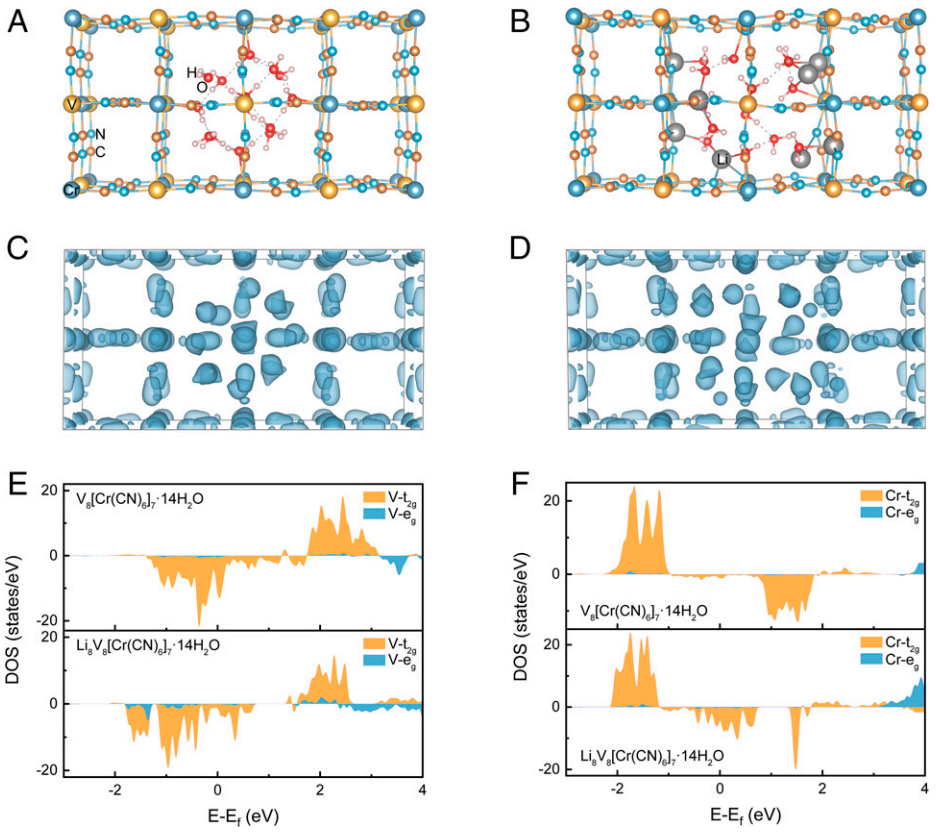

Fig. 4. DFT calculation for ionic control of magnetism. The atomistic structure model is viewed along the *c* axis for (*A*) $V_8[Cr(CN)_6]_7{\cdot}14H_2O$ and (*B*) $Li_8V_8[Cr(CN)_6]_7{\cdot}14H_2O$. The charge density map is viewed along the *c* axis for (*C*) $V_8[Cr(CN)_6]_7{\cdot}14H_2O$ and (*D*) $Li_8V_8[Cr(CN)_6]_7{\cdot}14H_2O$. Spin-polarized partial densities of states are projected onto *d* orbitals of (*E*) Cr and (*F*) V elements.

the orbitals of each atom. Due to the ligand field effect from the octahedral bonding environment for V and Cr atoms, 3d orbitals are separated into e_g and t_{2g} groups. The population in t_{2g} orbitals of Cr and V dominates the electronic states near the Fermi level. The spins on Cr and V orient antiferromagnetically, resulting in a net magnetic moment of 0.5247 μ_B per unit cell. The C, N, and Li elements show a negligible total polarization (*SI Appendix*, Fig. S6 and Table S4). After inserting Li cations, electrons from Li atoms fill the 3*d* orbitals of neighboring V atoms and convert their electron configurations into half-filled states, leading to an increase in the magnetic moments. 3*d* orbitals of neighboring Cr atoms become more than half-filled by electrons of Li atoms, resulting in the decrease in the magnetic moments. The dramatic change of magnetic moments is mainly induced by those magnetic atoms that are close to Li atoms and water molecules (*SI Appendix*, Table S4), due to the short-range nature of electron donation from Li atoms.

Room-temperature magneto-ionic coupling features in compound 1 promise to monitor real-time SOC in Li-ion batteries. As shown in Fig. 5*A*, we provide a magneto-ionic control pathway to enable the SOC estimation for a Li-ion battery consisting of Cu (current collector) + compound 1/separator/coplanar waveguide (CPW)/separator/Li + Cu (current collector). As shown in *SI Appendix*, Figs. S7–S9, an external static and alternating current (AC) magnetic field is applied to match the microwave frequency to excite the spin wave while the CPW is applied as the spin-sensing unit. The static magnetic field is aligned in-plane of the cathode material. The simulation shows that the CPW can generate a pronounced electromagnetic field around the sensing region (Fig. 5*B*). The derivative of the microwave absorption intensity (I) with respect to the magnetic field dI/dH (FMR signal) is measured when H and f fulfill the resonance condition of compound 1.

The resonance frequency does not shift during the lithiation (Fig. 3*D*), which enables a constant field to study the lithiation level. We select a 0.35-GHz microwave source and 100-Oe saturation magnetic field for the following studies. As shown in the top panel of Fig. 5*C*, the discharging-dependent FMR signal under different discharging rates is consistent, suggesting its accuracy and reliability. For a discharging level of 15 mAh g^{-1}, the FMR signal shows a subtle variation of 2.3% as the discharging rate increases from 1 to 10 C (*SI Appendix*, Fig. S10). As a comparison, we also present the traditional terminal voltage (potential between cathode and anode) method for the SOC estimation. As shown in the bottom panel of Fig. 5*C*, the terminal voltage changes significantly with the discharging rate. For a discharging level of 15 mAh g^{-1}, the terminal voltage displays a significant decrement of 51.7% as the discharging current is increased from 1 to 10 C (*SI Appendix*, Fig. S10), challenging for a precise SOC estimation. In addition, compared with the OCV method, the magneto-ionic cathode material–based real-time SOC estimation shows two advantages. First, a noncontact molecular magneto-ionic sensor, a cathode material, can provide real-time SOC estimation without the need of a long disconnection from the load. Second, a magneto-ionic sensor shows a fast response to the output change. As shown in Fig. 5*D*, when the cell is disconnected from the load, the FMR signal shows the response time of less than 1 min. However, the OCV drops drastically and then declines gradually after being disconnected from the load; therefore, a stable OCV could take more than 50 min for the SOC estimation (30, 31).

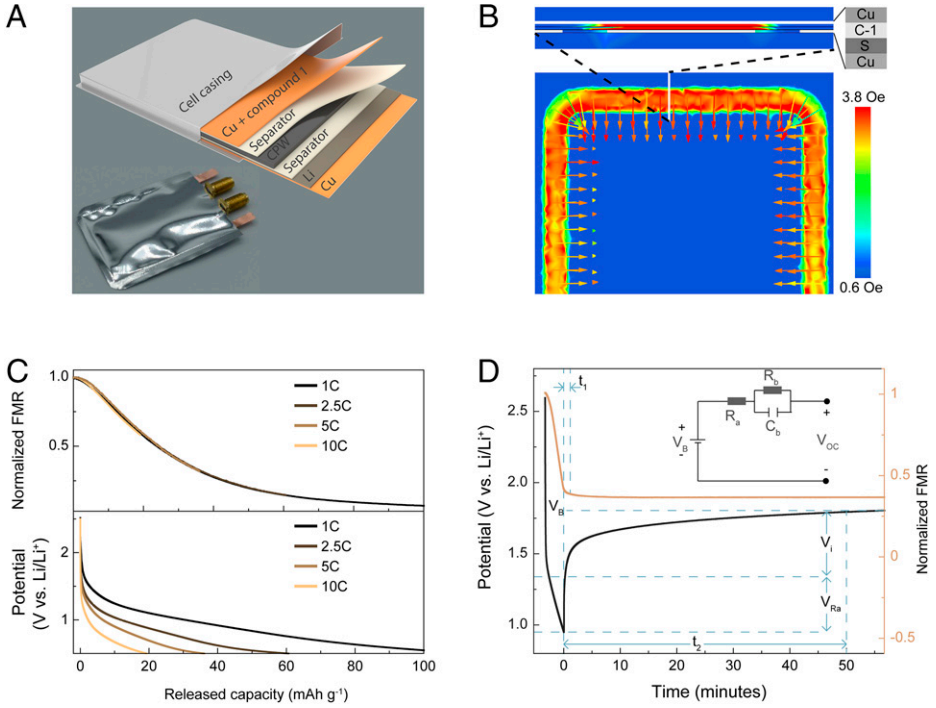

Fig. 5. Magneto-ionic cathode–based Li-ion battery for the SOC estimation. (*A*) Picture and structure of the RF magneto-ionic-based Li-ion battery. (*B*) Simulation for the distribution of microwave-generated magnetic field in the battery. C-1 and S represent Cu + compound 1 and separator, respectively. (*C*) Normalized FMR signal versus released capacity for compound 1 cathode inside the battery at different discharging rates. Potential versus released capacities for compound 1 cathode inside the battery at different discharging rates. (*D*) Time-dependent potential and FMR signal after the cell is disconnected from load. OCV = $V_B + V_i \cdot e^{(-t/R_b C_b)}$. V_B is the internal voltage; C_b is the lumped capacitance of the cell; V_i is the initial voltage across C_b and R_b; R_a is the integrated resistance of cell connections; and V_{Ra} is the voltage drop on R_a. The applied magnetic field and RF field are 100 Oe and 0.35 GHz, respectively. t_1 and t_2 indicate the response times for magneto-ionic electrode-based and OCV-based methods, respectively.

Conclusion. A molecular magneto-ionic cathode material in a rechargeable Li-ion battery is demonstrated, in which its structural vacancy and hydrogen-bonding networks enable the lithiation and delithiation for magneto-ionics, which in turn lead to real-time SOC monitoring in batteries. The magneto-ionic control of magnetism in compound 1, dynamic and reversible tunability of the T_c from 317 to 220 K, is further corroborated through the FMR and computational modeling studies. The microwave-excited spin wave in molecular magnetic cathode reveals the lithiation and delithiation levels, enabling a real-time magneto-ionic-based SOC in rechargeable batteries under a low magnetic field of 100 Oe and a RF of 0.35 GHz. The magneto-ionic-based sensor shows a more than 20× increase in accuracy and a more than 50× reduction in response time compared to the terminal voltage-based and OCV-based methods, respectively. It has to be mentioned that further studies could be performed in exploring new molecule-based magnetic electrodes with large capacities.

Materials and Methods

Magnetic Properties, Morphology, and Optical Characterization. Magnetic properties measurements are performed by vibrating sample magnetometer (MicroSense EZ7-380V). Scanning electron microscope (SEM) and energy-dispersive X-ray spectrometer (EDS) experiments are carried out in a Hitachi S4000 field emission SEM EDS. Agilent Cary 630 FTIR spectrometer is applied for FTIR measurement.

Thermal Analysis. Thermal analysis is carried out by a TA Instruments SDT Q600 Differential Calorimeter/Thermogravimetric Analyzer under N_2 atmosphere at 10 K min^{-1}.

FMR. FMR is performed by irradiation of a microwave using a continuous wave FMR system. The FMR system uses a microwave vector network analyzer (Agilent/HP 8719D; 0.05 to 13.5 GHz), which is then connected to a CPW with a sample kept in close proximity to the waveguide. The microwave absorption by the sample is measured via a phase-sensitive detection using a Schottky detector connected to the CPW. Field modulation to the static magnetic field is provided by Helmholtz coils, which are needed for locking detection. S_{21} parameter is measured with Agilent/HP 8719D.

Electrochemical Measurement. Electrochemical insertion/extraction of Li cations for compound 1 is performed in a half cell using 1 M $LiClO_4$ in propylene carbonate as an electrolyte and Li metal as a counterelectrode. Compound 1 is used as the working electrode, and Li metal is used as both the counter and working electrodes. A metrohm Autolab PGSTAT204 is used for all electrochemical measurements. Cyclic voltammetry curves were collected at 10 mV s^{-1} within the range of 0.5 to 2.5 V versus Li/Li^+. Coin-type batteries (CR2032) are prepared in an Ar-filled glove box for EIS tests. The coin cell is constructed by 3 mg compound 1, Li foils cathodes, 1 M $LiClO_4$ electrolyte, and a polypropylenes separator. EIS is measured from 100 kHz to 0.1 Hz and with an AC signal of 10 mV in amplitude as the perturbation at different direct current voltages.

DFT Calculations. To capture both covalent and hydrogen bonding interactions in the materials, first-principles calculations are performed in a 2 × 2 × 1 supercell using the strongly constrained and appropriately normed semilocal density functional (32) implemented in Vienna Ab initio Simulation Package code (33). The atomic structures are relaxed with a force tolerance of 0.01 eV $Å^{-1}$. An energy cutoff of 400 eV and a 2 × 1 × 1 reciprocal space grid with Monkhorst-Pack method (34) are used for all calculations. To take the strong correlation effect of transition metal elements into consideration, an effective Coulomb interaction is considered in the DFT+U framework with a $U = 1.0$ eV used for V atoms in the calculations. The optimal U value is referred to a recent work (35).

To understand the role of Li insertion in the magnetic properties of transition metal atoms in the supercell, we doped eight Li atoms in each supercell. Several possible doping configurations are considered, and the Li-doped supercell with

the lowest energy after structural relaxation is chosen for further self-consistent calculations.

Data Availability. All study data are included in the article and/or *SI Appendix*.

ACKNOWLEDGMENTS. The US Department of Energy, Office of Basic Energy Sciences, Division of Materials Sciences and Engineering supports S.R. (physical properties of materials) under award DE-SC0018631. The US Army Research Office supports the materials design under award W911NF-18-2-0202. This work was supported by New York State Energy Research and Development Authority under award 138126. W.G. and Q.Y. acknowledge support from the US Department of Energy, Office of Science, under award DE-SC0020310. The computational work benefitted from the supercomputing resources of the National Energy Research Scientific Computing Center, a US Department of Energy Office of Science User Facility operated under contract DE-AC02-05CH11231.

Author affiliations: [a]Department of Mechanical and Aerospace Engineering, University at Buffalo, The State University of New York, Buffalo, NY 14260; [b]Department of Physics, Temple University, Philadelphia, PA 19122; [c]Department of Materials Design and Innovation, University at Buffalo, The State University of New York, Buffalo, NY 14260; [d]Department of Chemistry, University at Buffalo, The State University of New York, Buffalo, NY 14260; and [e]Research and Education in Energy Environment & Water Institute, University at Buffalo, The State University of New York, Buffalo, NY 14260

1. A. J. Tan *et al.*, Magneto-ionic control of magnetism using a solid-state proton pump. *Nat. Mater.* **18**, 35–41 (2019).
2. U. Bauer *et al.*, Magneto-ionic control of interfacial magnetism. *Nat. Mater.* **14**, 174–181 (2015).
3. M. Gößler *et al.*, Magneto-ionic switching of superparamagnetism. *Small* **15**, e1904523 (2019).
4. H.-B. Li *et al.*, Electric-field control of ferromagnetism through oxygen ion gating. *Nat. Commun.* **8**, 2156 (2017).
5. H. Liu *et al.*, Organic-based magnon spintronics. *Nat. Mater.* **17**, 308–312 (2018).
6. H. Liu *et al.*, Spin wave excitation, detection, and utilization in the organic-based magnet, $V(TCNE)_x$ (TCNE = tetracyanoethylene). *Adv. Mater.* **32**, e2002663 (2020).
7. Y. Huang, S. Ren, Multifunctional Prussian blue analogue magnets: Emerging opportunities. *Appl. Mater. Today* **22**, 100886 (2021).
8. P. Perlepe *et al.*, Metal-organic magnets with large coercivity and ordering temperatures up to 242°C. *Science* **370**, 587–592 (2020).
9. H.-L. Cai *et al.*, Above-room-temperature magnetodielectric coupling in a possible molecule-based multiferroic: Triethylmethylammonium tetrabromoferrate(III). *J. Am. Chem. Soc.* **134**, 18487–18490 (2012).
10. P.-F. Li *et al.*, Organic enantiomeric high-T_c ferroelectrics. *Proc. Natl. Acad. Sci. U.S.A.* **116**, 5878–5885 (2019).
11. Y.-M. You *et al.*, An organic-inorganic perovskite ferroelectric with large piezoelectric response. *Science* **357**, 306–309 (2017).
12. S. Ohkoshi, K. Arai, Y. Sato, K. Hashimoto, Humidity-induced magnetization and magnetic pole inversion in a cyano-bridged metal assembly. *Nat. Mater.* **3**, 857–861 (2004).
13. Y. Mizuno *et al.*, Precise electrochemical control of ferromagnetism in a cyanide-bridged bimetallic coordination polymer. *Inorg. Chem.* **51**, 10311–10316 (2012).
14. C. Wang *et al.*, Magnetism tuned by intercalation of various metal ions in coordination polymer. *Chin. Chem. Lett.* **30**, 1390–1392 (2019).
15. S. Ohkoshi *et al.*, High proton conductivity in Prussian blue analogues and the interference effect by magnetic ordering. *J. Am. Chem. Soc.* **132**, 6620–6621 (2010).
16. Y. Hu *et al.*, Printing air-stable high-T_c molecular magnet with tunable magnetic interaction. *Nano Lett.* **22**, 545–553 (2022).
17. Y. Hu *et al.*, Proton switching molecular magnetoelectricity. *Nat. Commun.* **12**, 4602 (2021).
18. Q. Li *et al.*, Extra storage capacity in transition metal oxide lithium-ion batteries revealed by in situ magnetometry. *Nat. Mater.* **20**, 76–83 (2021).
19. Y. Gao *et al.*, Polymer-inorganic solid-electrolyte interphase for stable lithium metal batteries under lean electrolyte conditions. *Nat. Mater.* **18**, 384–389 (2019).
20. Y. Gao *et al.*, Interfacial chemistry regulation via a skin-grafting strategy enables high-performance lithium-metal batteries. *J. Am. Chem. Soc.* **139**, 15288–15291 (2017).
21. F. Yao *et al.*, Diffusion mechanism of lithium ion through basal plane of layered graphene. *J. Am. Chem. Soc.* **134**, 8646–8654 (2012).
22. L. Hedley, N. Robertson, J. O. Johansson, Electrochromic thin films of the V-Cr Prussian blue analogue molecular magnet. *Electrochim. Acta* **236**, 97–103 (2017).
23. O. Sato, T. Iyoda, A. Fujishima, K. Hashimoto, Electrochemically tunable magnetic phase transition in a high-Tc chromium cyanide thin film. *Science* **271**, 49–51 (1996).
24. A. Simonov *et al.*, Hidden diversity of vacancy networks in Prussian blue analogues. *Nature* **578**, 256–260 (2020).
25. P. Nie *et al.*, Prussian blue analogues: A new class of anode materials for lithium ion batteries. *J. Mater. Chem. A Mater. Energy Sustain.* **2**, 5852–5857 (2014).
26. L. Shen, Z. Wang, L. Chen, Prussian blues as a cathode material for lithium ion batteries. *Chemistry* **20**, 12559–12562 (2014).
27. Y. Huang *et al.*, Cross-linking and charging molecular magnetoelectronics. *Nano Lett.* **21**, 4099–4105 (2021).
28. E. Dujardin *et al.*, Synthesis and magnetization of new room-temperature molecule-based magnets: Effect of stoichiometry on local magnetic structure by X-ray magnetic circular dichroism. *J. Am. Chem. Soc.* **120**, 11347–11352 (1998).
29. X. Wu *et al.*, Diffusion-free Grotthuss topochemistry for high-rate and long-life proton batteries. *Nat. Energy* **4**, 123–130 (2019).
30. Z. M. Salameh, M. A. Casacca, W. A. Lynch, A mathematical model for lead-acid batteries. *IEEE Trans. Energ. Convers.* **7**, 93–98 (1992).
31. S. Lee, J. Kim, J. Lee, B. H. Cho, State-of-charge and capacity estimation of lithium-ion battery using a new open-circuit voltage versus state-of-charge. *J. Power Sources* **185**, 1367–1373 (2008).
32. J. Sun, A. Ruzsinszky, J. P. Perdew, Strongly constrained and appropriately normed semilocal density functional. *Phys. Rev. Lett.* **115**, 036402 (2015).
33. G. Kresse, J. Furthmüller, Efficient iterative schemes for ab initio total-energy calculations using a plane-wave basis set. *Phys. Rev. B Condens. Matter* **54**, 11169–11186 (1996).
34. H. J. Monkhorst, J. D. Pack, Special points for Brillouin-zone integrations. *Phys. Rev. B* **13**, 5188 (1976).
35. O. Y. Long, G. S. Gautam, E. A. Carter, Evaluating optimal U for 3d transition-metal oxides within the SCAN+U framework. *Phys. Rev. Mater.* **4**, 045401 (2020).
36. O. Sato, Electrochromism and electrochemical magnetism in Ni–Fe Prussian blue. *J. Solid State Electrochem.* **11**, 773–779 (2007).